An Investigation of In Vitro Bioactivities and Cytotoxicities of Spray Pyrolyzed Apatite Wollastonite Glass-Ceramics

Andualem Belachew Workie [1], Henni Setia Ningsih [1], Wen-Ling Yeh [2,3,4,*] and Shao-Ju Shih [1,5,*]

1 Department of Materials Science and Engineering, National Taiwan University of Science and Technology, 43, Sec. 4 Keelung Road, Taipei 10607, Taiwan; d10904804@mail.ntust.edu.tw (A.B.W.); hennisetianingsih@gmail.com (H.S.N.)

2 Department of Orthopeadic, Lotung Poh-Ai Hospital, No. 81, Nanchang Road, Yilan 26546, Taiwan

3 Department of Medicine, Chang Gung University, No. 259, Wenhua 1st Road, Taoyuan 33302, Taiwan

4 Department of Orthopeadic, Linkou Chang Gung Memorial Hospital, No. 5, Fuxing Road, Taoyuan 33373, Taiwan

5 Department of Fragrance and Cosmetic Science, Kaohsiung Medical University, No. 100, Shih-Chuan 1st Road, Kaohsiung 80708, Taiwan

* Correspondence: pelewly@cgmh.org.tw (W.-L.Y.); shao-ju.shih@mail.ntust.edu.tw (S.-J.S.); +886-2-27303716 (ext. 5421) (W.-L.Y.); +886-2-27303716 (S.-J.S.)

Abstract: An apatite-wollastonite glass ceramic (AWGC) has been recognized as one of the popular bioactive materials due to its good osteoconductivity and high mechanical properties in the field of tissue engineering. Various processes have been developed to fabricate AWGCs. Among them, the sol-gel process is one of the most popular processes. However, sol-gel has the drawbacks of discontinuous processing and long processing time, making it unsuitable for mass production. This study demonstrates a successful synthesis of AWGCs using a spray pyrolysis method to overcome these drawbacks, and the prepared pellets were sintered at temperatures of 700, 800, 900, 1000, and 1100 °C for four hours. In addition, X-ray diffraction, scanning electron microscopy, and X-ray energy-dispersive spectroscopy were used to obtain the phase composition, morphology, and chemical information of AWGCs. For bioactive measurements, among these AWGC samples, the 1100 °C sintered sample reveals the highest bioactivity. The MTT result indicates that all AWGCs are not non-toxic to the MC3T3-E1 cells and increase the growth rate of MC3T3-E1 cells.

Keywords: apatite-wollastonite glass ceramic; bioactivity; spray pyrolysis; biocompatibility

1. Introduction

Bioactive ceramics, exhibiting superior osteoconductive properties and having the ability to direct bonding to bone tissue [1], have been widely used for the fields of dental implants [2]. The most common materials are bioglass, synthetic hydroxyapatite (HA), beta-tricalcium phosphate, and apatite-wollastonite glass ceramics (AWGCs). Among these materials, AWGCs, with the compositions of 4.6 wt% MgO, 44.7 wt% CaO, 34.0 wt% SiO_2, 16.2 wt% P_2O_5, and 0.5 wt% CaF_2 and containing the two crystalline phases of apatite and wollastonite, were invented by Kokubo et al. in 1982 [3]. For clinical applications (e.g., hip revisions), several problems have been reported for the common synthetic HA [4]. For example, the phenomena of bone bonding and gap filling have been found nearly one year after implantation, which suggests the low bioactivity and low osteoconductivity of HA [4]; it takes some time for the patient to start weight bearing after surgery, which implies the mechanical strength of HA is too weak. Therefore, the main purpose of Kokubo et al. is to develop novel bioceramic materials with better bioactivity and higher mechanical strength than the common HA. Furthermore, Kukubo showed that the AWGCs withstand the bending stress of 65 MPa in the human body environment for over 10 years [5]. In addition, the synthetic HA often breaks in situ after surgery directly below the iliac crest, whereas

seldom cases have been observed for AWGCs (97% of the patients are satisfied with the AWGC-made iliac crest prosthesis) [6]. Therefore, the preparation of high osteoconductive AWGC materials is urgent and critical for the development of future bioceramic materials.

Due to the importance of AWGC materials, various processes, including the solid-state method [7,8] and sol-gel [9,10], have been employed to synthesize AWGCs. The conventional melt-quenching method for preparing AWGC was proposed by Kokubo et al. [3], and the method contains two steps of formation of a glass matrix by melt-quenching and crystallization of apatite and wollastonite phases by heating treatments; the detailed procedure is provided in the previous study [11]. The major advantage of the solid-state method is its feasibility for mass production; however, the method involves the disadvantages of difficulty in maintaining high purity [12], and requiring high treating temperature [13]. So, for solving the above problems, the sol-gel method has been proposed to synthesize AWGC materials. Initially, since the heat treatment of sol-gel is relatively lower than the conventional melt-quenching method, it is possible for sol-gel-derived glass ceramics to remove the components with the aim of decreasing the melting temperature (e.g., Na_2O) [14]. Furthermore, the sol-gel derived materials offer the other advantages of higher purity and homogenous [13]. Although the sol-gel method is so popular, the sol-gel method has the drawbacks of discontinuous processing, long processing time (~1–2 days), and unsuitability for mass production [15]. Spray pyrolysis (SP) has the advantages of high purity, homogenous, and continuous processing [16]; these advantages overcome the disadvantages of high contamination and non-homogenous for the conventional melt-quenching method and the disadvantage of non-continuous for the sol-gel method. In addition, to the best of the authors' knowledge, a rare study has been conducted to synthesize AWGC materials using spray pyrolysis. So, the SP method is chosen in this study.

In this study, the spray pyrolyzed AWGC starting powder calcined at 700 °C was manufactured, and then the AWGC sintered samples were synthesized at the sintering temperatures of 700, 800, 900, 1000, and 1100 °C. For characterization, X-ray diffraction (XRD), scanning electron microscopy (SEM), nitrogen absorption-desorption technique, and X-ray energy-dispersive spectroscopy (XEDS) were used to analyze the phase compositions, surface morphologies, specific surface areas, and chemical compositions of both starting powder and sintered samples. Both techniques of XRD and SEM were used to investigate the in vitro bioactivities of AWGCs. In addition, the cytotoxicities of MC3T3-E1 cells for AWGCs were examined using 3-(4,5-dimethylthiazol-2-yl)-2,5-diphenyltetrazolium bromide (MTT). Finally, the microstructure, bioactivity, and cytotoxicity were correlated with the sintering conditions of spray-pyrolyzed AWGCs.

2. Materials and Methods

2.1. Preparation and Characterization of AWGC Starting Powder

In this experiment, the starting powder of AWGC was synthesized using spray pyrolysis. Briefly, the AWGC powder was prepared according to Kokubo et al. [3] with the composition ratio of $MgO:CaO:SiO_2:P_2O_5:CaF_2$ is 4.6:44.7:34.0:16.2:0.5 in weight percent, respectively. The precursor solution consisted of 11.79 g of tetraethyl orthosilicate (TEOS) (98.0%, Thermo Scientific, Waltham, MA, USA), 18.82 g of calcium nitrate tetrahydrate (CNT) (98.5%, Showa, Tokyo, Japan), 2.93 g of magnesium nitrate hexahydrate (MgN) (99.0%, Acros organics, Geel, Belgium), 4.16 g of triethyl phosphate (TEP) (99.0%, Thermo scientific, Ward Hill, MA, USA), and 0.05 g of calcium fluoride (CaF_2) (99.0%, Sigma Aldrich, Steinheim, Germany). After mixing all the above precursors (i.e., TEOS, CNT, MgN, TEP, and CaF_2) in 500 mL of deionized water, 20.49 g of glacial acetic acid (98.0%, Echo, Wunstorfer, Germany) was added as the catalyst, and this precursor solution was stirred for 30 min at 25 °C. Next, the homogeneous precursor solution was atomized using an ultrasonic atomizer (King Ultrasonic, KT-100A, New Taipei, Taiwan) with a vibration frequency of 1.65 MHz to generate droplets. Afterward, the resulting droplets were sprayed into a tubular quartz furnace (Dengyng, D110, New Taipei, Taiwan) with a length of 1200 mm and an inner diameter of 30 mm. The furnace was heated using three zones of evaporation

(250 °C), calcination (700 °C), and decomposition (350 °C). Finally, the starting powder was collected and dried at 80 °C in an oven overnight to remove excess water.

For characterization, the chemical composition of AWGC starting powder was identified using an X-ray diffractometer (D2 Phaser, Bruker, Karlsruhe, Germany) with the Cu Kα radiation (λ = 1.5405 Å). The XRD pattern was obtained by scanning the starting powder through 2θ from 20° to 80°. Next, the field emission scanning electron microscope (JSM-6500F, JEOL, Tokyo, Japan) equipped with XEDS was employed to observe the surface morphology and chemical composition of AWGC starting powder. The SEM sample was prepared by dropping a small amount of AWGC starting powder on the carbon tape and coated with platinum for 30 s to minimize the charging effect. For the specific surface area measurement, the AWGC starting powder was measured according to Brunauer-Emmett-Teller (BET) method using the nitrogen adsorption/desorption analyzer (Novatouch LX2, Quantachrome, Boynton Beach, FL, USA).

2.2. Fabrication and Characterization of Sintered AWGC Samples

To fabricate the sintered AWGC samples, ~0.12 g of AWGC starting powder was uniaxially compressed at 60 MPa to form green pellets with ~10 mm diameter and ~2.5 mm thickness. Next, the prepared pellets were sintered at the temperatures of 700, 800, 900, 1000, and 1100 °C with a heating rate of 5 °C/min and a sintering time of 4 h in the furnace (D110, Dengyng, New Taipei, Taiwan).

For crystallographic information, the XRD was utilized to investigate crystalline structures and crystallite sizes of AWGC sintered samples. The average crystallite sizes *(L)* of AWGC samples were estimated using the Scherrer formula as given below:

$$L = \frac{K\lambda}{B\cos\theta} \qquad (1)$$

where *L* is crystallite size, *K* is the constant of 0.89, λ is the Cu Kα radiation wavelength of 1.5405 Å, *B* is the full-width half maximum (FWHM) of individual XRD peaks, and θ is the diffraction angle. Furthermore, the morphologies of various sintered AWGC were characterized by SEM. The bulk densities of sintered AWGC samples were measured according to Archimedes's principle with the formula below:

$$\rho = \rho_w \frac{W_d}{(W_a - W_b)} \qquad (2)$$

where ρ is the density of the samples and ρ_w is the density of water (1.00 g/cm^3). Additionally, W_d, W_a, and W_b are dry weight, saturated weight, and suspended weight of the samples, respectively.

For bioactivities, the pellets of AWGC were placed into the containers with 50 mL of simulated body fluid (SBF) solution and incubated for 21 days at 37 °C. In terms of bioactive properties, the surface deposition of the hydroxyapatite layer on the AWGC was observed by XRD and FESEM.

Finally, the MTT assay (Gibco, Waltham, MA, USA) was performed to evaluate the cell viability of all sintered AWGC samples. For the cell viability test, the MC3T3-E1 cells (American Type Culture Collection no. CRL-2594, Manassas, VA, USA) were cultured in a polystyrene plate with MEM-α medium (Gibco, Waltham, MA, USA) supplemented with 10% fetal bovine serum (Gibco, Waltham, MA, USA) and penicillin-streptomycin (10.000 U/mL) (Gibco, Waltham, MA, USA) at 37 °C in a humidified atmosphere with 5% carbon dioxide. Afterward, the cells were transferred and seeded into 24 well plates with 2×10^4 cells per well in a volume of 500 μL. Next, the extraction of AWGC sintered sample and MEM-α medium (5 mg/mL) were added and incubated for 72 h at 37 °C in the incubator with 5% of carbon dioxide. The control group consisted of MC3T3-E1 cells, which were seeded in 24 well plates without any AWGC sample. After 72 h of incubation, 300 μL of the MTT solutions were added and kept for 4 h. Then, the supernatants were removed

and 200 μL of dimethyl sulfoxide (Fisher Chemical, Fair Lawn, NJ, USA) solutions were added to dissolve the crystal formazan, and the absorbance was determined at 570 nm by using a microplate reader (Multiskan Go, Thermo Scientific, Waltham, MA, USA).

3. Results

In this study, two steps were required for AWGC fabrication. First, the AWGC starting powder was prepared using SP, and then the AWGC raw powder was sintered to form AWGC samples using a furnace. Figure 1 shows the phase composition and particle morphology of as-prepared AWGC starting powder using spray pyrolysis. Initially, Figure 1a shows the XRD pattern of the as-prepared powder from the spray pyrolysis calcination at a temperature of 700 °C; the pattern suggests that the powder is composed of glass and crystalline phase. Initially, the bump between the diffraction angles of 20 and 60° suggests the existence of an amorphous structure. Then, for the crystalline phase, the main phase hydroxylapatite (JCPDS number 86-0740) and the minor phase of SiO_2 (JCPDS number 75-1555) have been detected. In the pattern, the hydroxylapatite phase reveals the crystal planes of (102), (210), (211), (112), (300), (212), (131), and (222) with the diffraction angles of 26.2, 28.7, 31.9, 40.0, 41.6, 46.8, and 49.1°, respectively. The minor SiO_2 phase only shows the (101) plane (with a diffraction angle of 22.3°). The micrograph of the as-received powder is shown in Figure 1b; from the image, the particles have a particle size of 0.92 ± 0.44 μm. Furthermore, the as-prepared powder exhibits the particle morphology of a smooth sphere. In addition, the XEDS measurement reveals the starting powder contains 35.00 ± 1.16 mol% Ca, 11.10 ± 0.02 mol% Mg, 10.80 ± 0.53 mol% P, 40.10 ± 2.17 mol% Si, and 3.00 ± 1.93 mol% F, which is close to the precursor composition (36.23 mol% Ca, 13.70 mol% Mg, 13.74 mol% P, 35.30 mol% Si, and 1.03 mol% F). In short, the XRD and SEM results suggest that the starting powder has been obtained using spray pyrolysis.
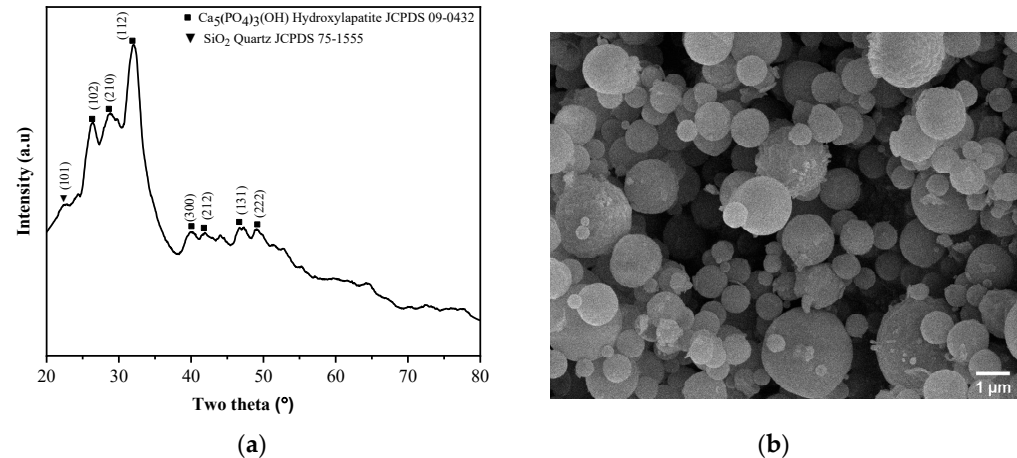
Figure 1. (**a**) XRD pattern, and (**b**) SEM micrograph of as-prepared starting powder using spray pyrolysis.

Figure 2 shows XRD patterns of the specimens sintered at temperatures of 700, 800, 900, 1000, and 1100 °C for four hours. These patterns appear as a mixture of glassy and crystalline phases in all specimens. Firstly, for the 700 °C sintered sample, three crystalline phases of wollastonite (JCPDS number 84-0654), whitlockite (JCPDS number 13-0404), and hydroxylapatite (JCPDS number 15-0876) have been identified, and the three largest peaks corresponding to (120) for the wollastonite phase, (300) for the whitlockite phase, and (112) for the hydroxylapatite phase with the diffraction angles of 30.35, 35.02, and 31.52°, respectively. In addition, similar spectra have been obtained for the 800, 900, 1000, and 1100 °C sintered specimens. Although all XRD patterns reveal the same phases, the relative intensities of these three phases change with the increasing sintering temperature. From Figure 2, it is clear that the main phase of hydroxylapatite is observed in the samples of phase 700 and 800 °C, but the dominant phase changes from hydroxylapatite to wollastonite in the sintered samples of 900, 1000, and 1100 °C.
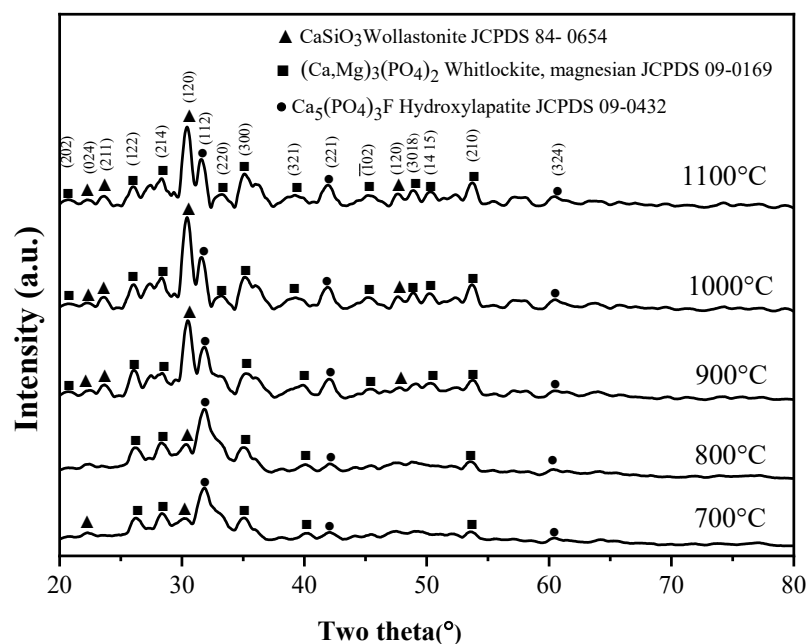
Figure 2. XRD patterns of AWGC samples sintered at the temperatures of 700, 800, 900, 1000, and 1100 °C for four hours.

Figure 3 shows the SEM micrographs of specimens sintered at temperatures of 700, 800, 900, 1000, and 1100 °C for four hours. For the 700 °C sintered specimens, (Figure 3a) most grains have a similar shape and similar shape to a sphere, such as the as-prepared powder (as shown in Figure 1b). A few grains are connected with a small neck area; this suggests that the 700 °C sintered AWGC sample is in the early stage of sintering. Figure 3b,c shows that more grains are connected to each other, and their shape changes from sphere to ellipse, when the sintering temperature increases to 800 °C and 900 °C; also, there is no obvious difference in grain size for 800 °C and 900 °C sintered samples. When the sintering temperature increases to 1000 °C, as shown in Figure 3d, all the grains become larger, and the pores become smaller; this micrograph suggests that the grain growth occurs obviously; from the figure, instead of an ellipse shape, all grains exhibit the irregular shape. A similar microstructure has been detected in the 1100 °C sintered AWGC sample in Figure 3e. Furthermore, the BET data of AWGC sintered at 700, 800, 900, 1000, and 1100 °C, and the corresponding values decreasing along with the increment of sintering temperature indicate as 25.71 ± 2.09, 23.82 ± 2.01, 15.63 ± 1.05, 10.54 ± 1.01, and 9.13 ± 1.05 m^2/g, respectively, as shown in Table 1. From the data, the specific surface area decreases with increasing sintering temperatures.

Table 1. Specific surface areas of AWGC samples sintered at temperatures of 700, 800, 900, 1000, and 1100 °C for four hours.

Sintering Temperature (°C)	Specific Surface Area (m^2/g)
700	25.71 ± 2.09
800	23.82 ± 2.01
900	15.63 ± 1.05
1000	10.54 ± 1.01
1100	9.13 ± 1.05

Density measurements of the spray pyrolyzed powders sintered at temperatures from 700 °C to 1100 °C for four hours are presented in Figure 4. According to the Archimedes method, the average density values and the corresponding standard deviation values of 700, 800, 900, 1000, and 1100 °C sintered specimens are 2.01 ± 0.02, 2.35 ± 0.02, 2.62 ± 0.02, 2.81 ± 0.02, and 2.70 ± 0.02 g/cm^3, respectively; from the figure, the density of specimens

increases from 700 °C to 1000 °C, and the maximum density is obtained at 1000 °C. Since the higher the bulk density (less porosity) the smaller the specific surface area, our density measurements are in agreement with the data of the specific surface area.
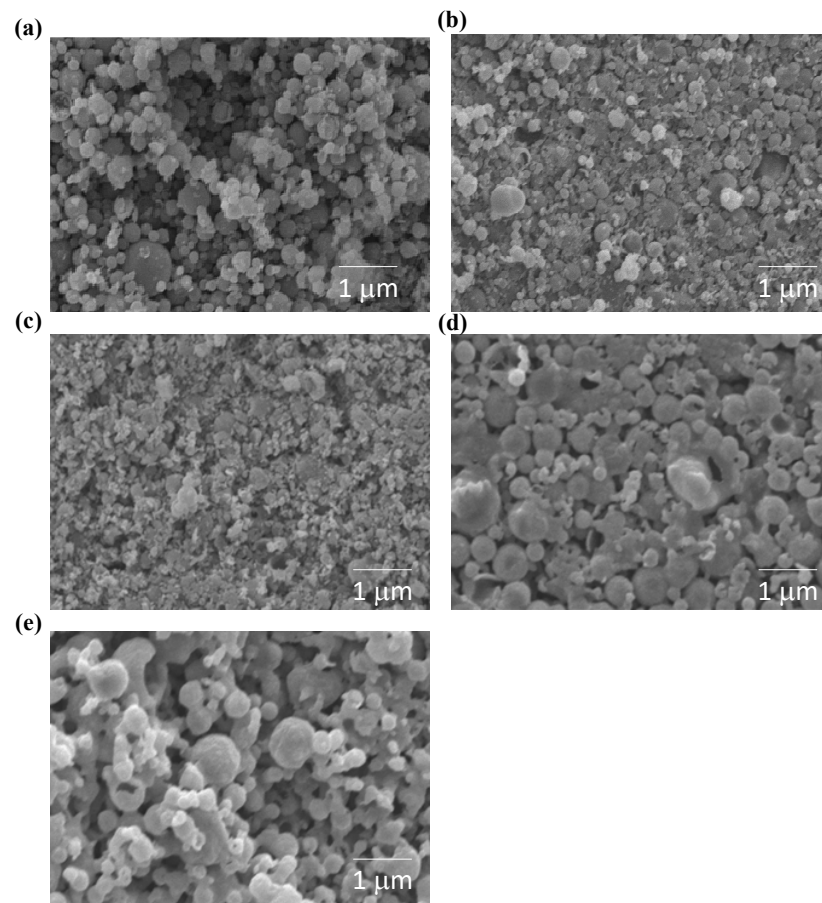

Figure 3. SEM micrographs of AWGC samples sintered at the temperatures of (**a**) 700, (**b**) 800, (**c**) 900, (**d**) 1000, and (**e**) 1100 °C for four hours.
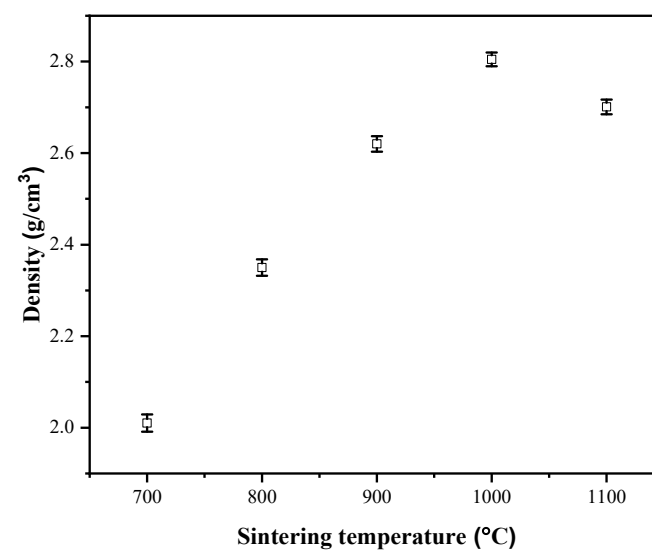
Figure 4. The bulk density of AWGC sample sintered at the temperatures of 700, 800, 900, 1000, and 1100 °C.

It is well known that bioactivity is directly related to the formation rates of hydroxyapatite crystals in SBF [17]. So, the XRD patterns of various AWGC before and after immersion (21 days) in SBF are shown in Figures 2 and 5, respectively. Firstly, for the immersed 700 °C sintered sample, the same crystalline phases of wollastonite, whitlockite, and hydroxyapatite, compared to the case of before immersion, have been identified. Additionally, the immersed 800, 900, 1000, and 1100 °C sintered AWGC samples show similar phase compositions as the cases before immersion. Due to the bioactivities of AWGC samples, the hydroxyapatite phase becomes the dominant phase in all samples. For calculation of the hydroxyapatite formation rates, the calculated crystalline sizes for the before- and after-soaked AWGC samples are shown in Table 2; from the table, it is clear that all immersed AWGC samples exhibit the larger hydroxylapatite crystal than that of the before-immersed AWGC samples, which indicates all samples have the bioactivity. Among these samples, the 1100 °C sintered sample reveals the highest bioactivity (an increase of 25.57% for hydroxylapatite crystal) rather than that (an increase of smaller than 8.50% for hydroxyapatite crystal) of the other sintered samples.
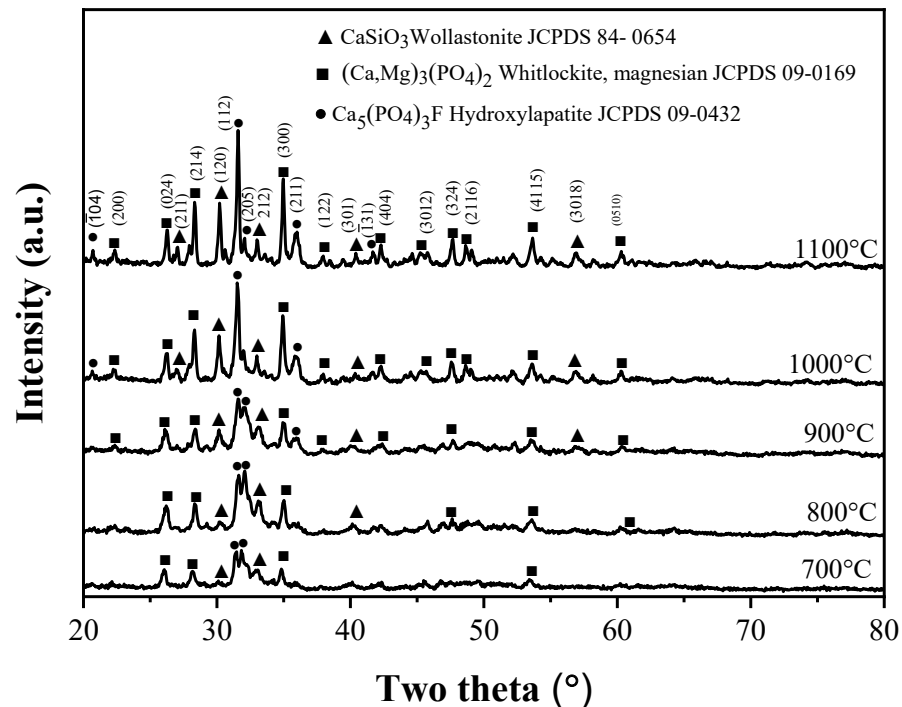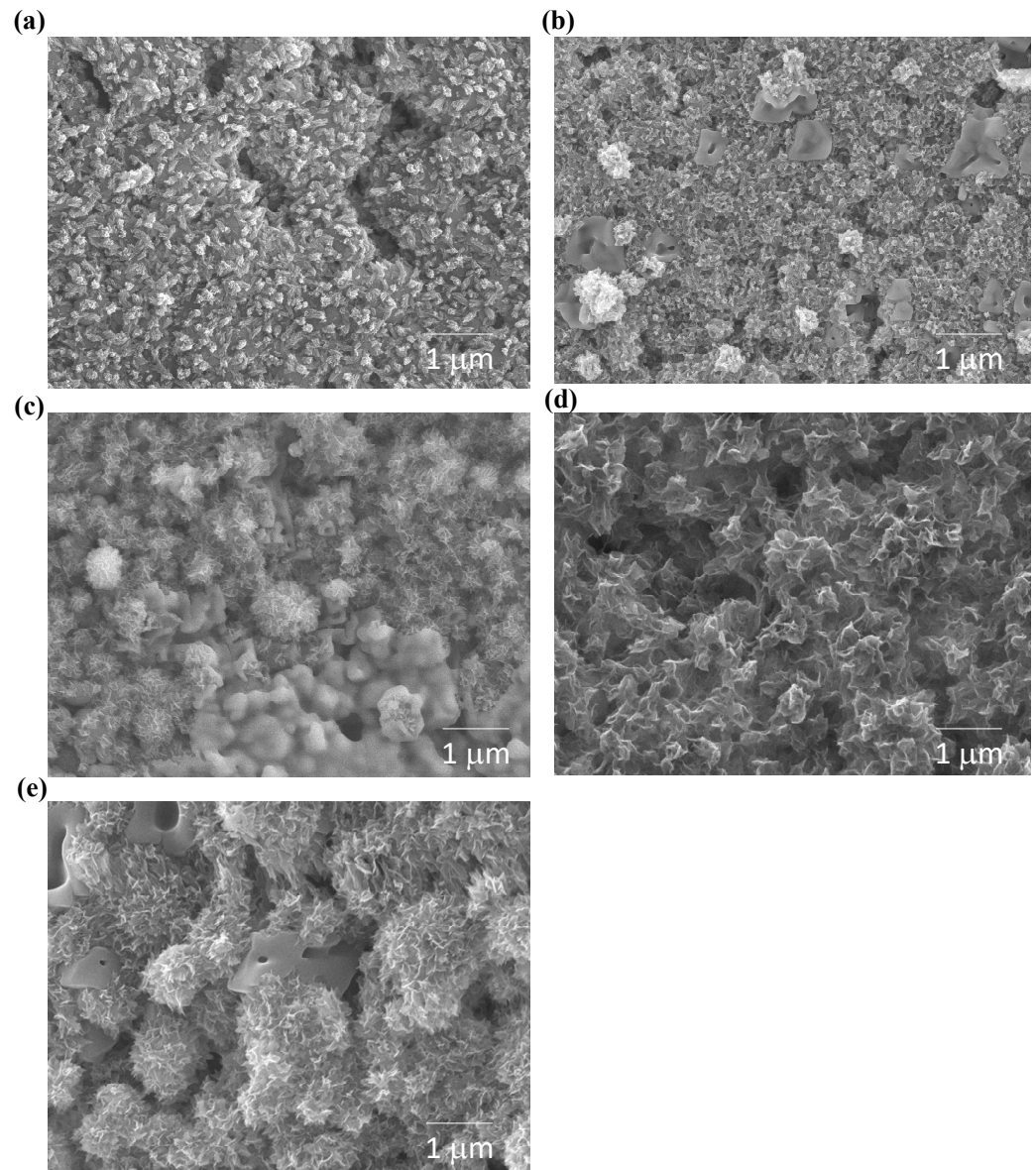

Figure 5. XRD patterns of AWGC samples sintered at the temperatures of 700, 800, 900, 1000, and 1100 °C for four hours after soaking in SBF for 21 days.

Table 2. Average crystallite sizes of apatite in AWGC samples sintered at temperatures of 700, 800, 900, 1000, and 1100 °C and soaked in SBF for 0 and 21 days.

| Sintering Temperature (°C)	Average Crystallite Size (nm)	
	0 Day of Soaking	21 Days of Soaking
700	25.41 ± 0.05	26.01 ± 0.15
800	28.76 ± 0.22	29.27 ± 0.43
900	32.15 ± 0.13	34.83 ± 0.26
1000	35.42 ± 0.14	37.56 ± 1.54
1100	36.79 ± 0.51	46.21 ± 1.62

Figure 6 shows the in vitro bioactivity measurements of various sintered AWGC specimens using SEM. Initially, for the 700 °C sintered sample, unlike the unsoaked condition (see Figure 3a), some small crystallites of ~25.4 nm have been observed on the AWGC

surface (see Figure 6a). Additionally, similar crystallites have been obtained for the 800 °C sintered specimens from the SEM images, as shown in Figure 6b. In addition, the SEM images of the 900, 1000, and 1100 °C samples show the needle-like structures in Figure 6c–e, respectively; from the figures, the density and size of needle-like crystals increase with the increasing sintering temperature.

(a)

(b)

(c)

(d)

(e)

Figure 6. SEM images of AWGC samples sintered at the temperatures of (**a**) 700, (**b**) 800, (**c**) 900, (**d**) 1000, and (**e**) 1100 °C after being soaked in SBF for 21 days.

The results of a study on the effects of sintering temperature on the biocompatibility of AWGC powders with MC3T3-E1 cells are presented in Figure 7. The statistical analysis shows that all sintered AWGC samples are significant differences (* $p < 0.05$) between the control sample. Initially, the cell viability of the 700 °C sintered sample was measured as $58.1 \pm 2.9\%$, which is slightly lower than the standard level of 70% (ISO 10993-5) [18], which, hence, is considered toxic to MC3T3-E1 cells. Although the 800, 900, 1000, and 1100 °C sintered samples still show a significant difference, their cell viability is much higher than 70%, which indicates that these samples are not non-toxic to the MC3T3-E1 cells and increase the growth rate of MC3T3-E1 cells.
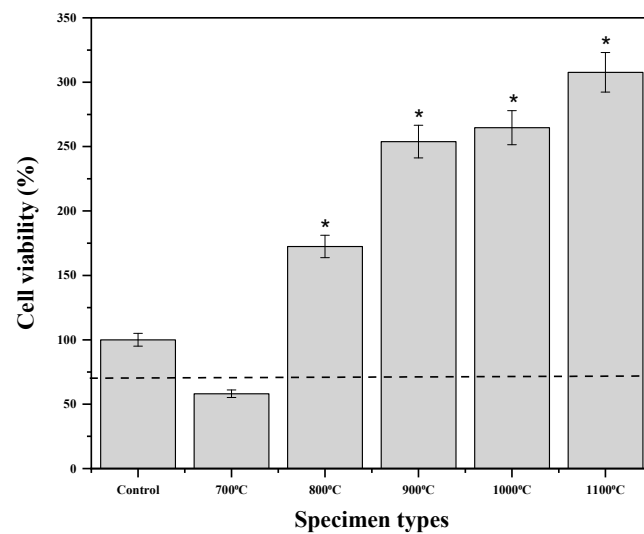
Figure 7. Cell viability test of AWGC samples sintered at the temperatures of 700, 800, 900, 1000, and 1100 °C for 72 h (* presents the statistical differences with respect to control, n = 3 and $p < 0.05$).

4. Discussion

The starting powder of AWGC exhibits the small crystallinity of hydroxylapatite and SiO_2 phases, according to the result of XRD as shown in Figure 1a. Since the crystallinity of our starting powder is weaker than that of AWGC prepared by Kitsugi et al. [19], and the main reason is that the short calcination time of spray pyrolysis (~10 s) at the temperature of 700 °C [20], and AWGCs may not have enough time for crystal growth. For the SEM analysis (see Figure 1b), the starting powder has an average particle size of 0.92 ± 0.44 µm, and the powder exhibits the two typical shapes of a smooth sphere and rough sphere, which is similar to our previous spray pyrolysis study of bioglass [21]. Additionally, the XEDS measurement revealed that the as-prepared powder contained 36.00 ± 1.16 mol% Ca, 9.73 ± 0.02 mol% Mg, 22.09 ± 0.53 mol% P, 31.10 ± 2.17 mol% Si, and 1.08 ± 0.03 mol% F, which is close to the precursor composition.

The changes in crystalline sizes and morphologies for various sintered AWGC samples are discussed. For crystalline size analysis, Table 2 reveals the average crystallite sizes of apatite in AWGC samples sintered at temperatures of 700, 800, 900, 1000, and 1100 °C and soaked in SBF for 0 and 21 days. First, for the un-immersed samples, the crystalline size increases with increasing sintering temperature (25.4 nm for the 700 °C case and 36.8 nm for the 1100 °C case). A higher sintering temperature provides more energy for grain boundary movement to increase grain size for larger crystalline sizes. Second, after 21 days' immersion in SBF, all samples show a larger crystalline size, which suggests that SBF induces the grain growth of apatite in all AWGC samples for the bioactivities. Furthermore, from our SEM images, rare needle-like apatite crystals from the un-immersed AWGC samples (see Figure 3), but more needle-like apatite crystals have been observed for the 21-day-immersed AWGC samples (see Figure 6). So, the SEM data are in agreement with the XRD patterns. Furthermore, the description of the wollastonite and whitlockite phases is shown below. For the wollastonite phase, with the composition of 4.6 wt% MgO, 44.7 wt% CaO, 34.0 wt% SiO_2, 16.2 wt% P_2O_5, and 0.5 wt% CaF_2, the wollastonite precipitated homogeneously in the AWGC sample at the temperature of 870 °C [22]. In addition, for the whitlockite phase, under sintering conditions, the magnesium ions might react with phosphate ions generated during the breakdown of precursor chemicals. This interaction between magnesium and phosphate species results in the formation of whitlockite. It is worth noting that this reaction incorporates magnesium ions into the apatite structure for the whitlockite phase [23].

In addition, for the morphology, when the sintering temperature increases from 700 to 1000 °C, more energy is provided for the AWGC samples for sample densification, which

results in the increase of bulk density (decreasing porosity). At 700 °C, most of the grains of AWGC have point contact with the neighboring grains, and therefore the existence of a lot of irregular pores results in the low density of AWGC. When the sintering temperature increases, AWGC grains receive more energy for grain growth, the point contacts of AWGC grains change to area contacts, and then their pore size decreases. Furthermore, a portion of the nanostructure decreases with increasing sintering temperature. In addition, the driving force for sintering in this study is the reduction of the surface free energy of the AWGC sample. The reduction in energy is accomplished by atom diffusion processes that lead to either "densification", by transporting matter from the grains into the pores, or "coarsening" of the microstructure, by rearrangement of matter between the particle surfaces without a decrease in the pore volume [24]. The decrease in the specific surface area for AWGC samples is mainly contributed by the densification that AWGC grains transport matters into the pores for the pore size decrease. However, the density of 1100 °C is lower than that of 1000 °C. The possible reason is that the intragranular porosity is increased. When the crystal growth rate is very high, pores may be left behind by rapidly moving boundaries. So, the pores are trapped inside the grains to induce discontinuous grain growth for lower bulk density [25].

For the cytotoxicity, the MTT assay shown in Figure 7 indicates that the specimen calcined at 700 °C exhibits toxicity against osteoblastic cells, whereas the 800, 900, 1000, and 1100 °C sintered AWGC samples were not. According to previous studies, the main factors, including phase compositions [26] and specific surface area [27], play a critical role in the cytotoxicity of bioceramics. Initially, let's consider the factor of phase composition; according to the XRD data (see Figure 2), all sintered AWGC samples exhibit the three main phases of wollastonite, whitlockite, and hydroxyapatite, which shows no obvious existence of a toxic phase to induce the lower level of 58.1% for the MTT assay. So, the result indicates the phase composition does not influence the cytotoxicity in this study. On the other hand, the toxic sample of 700 °C sintered AWGC sample has a higher proportion of nanostructures than the other AWGC samples, as shown in Figure 3, and this sample exhibits the highest specific surface area of 25.71 m^2/g (see Table 1). Therefore, this nanostructure may inhibit the mineralization of osteoblast culture [27] and impact cell adhesion and proliferation [28]. In addition, the relationship between specific surface area and cytotoxicity has been revealed in Figure 8. The specific surface areas of 9.13, 10.54, 15.63, 23.82, and 25.71 m^2/g are corresponding to the MTT value of 307.68, 264.70, 253.89, 172.47, and 58.14%, respectively. The result reveals that AWGC samples with a lower specific surface area give a higher MTT value (lower cytotoxicity).
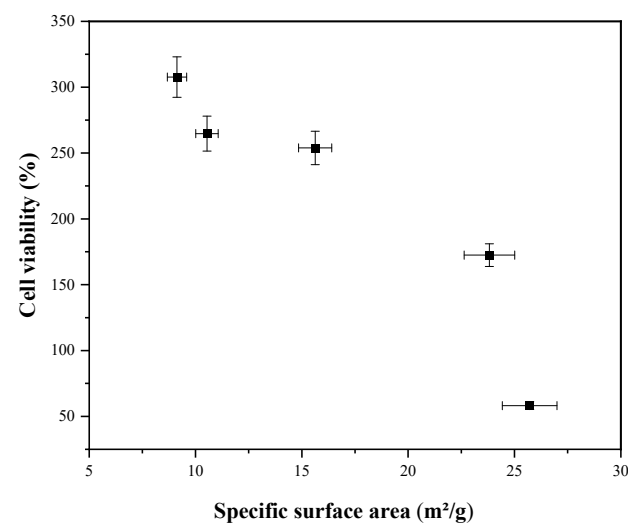
Figure 8. Correlation between specific surface area and cell viability of AWGC samples sintered at the temperatures of 700, 800, 900, 1000, and 1100 °C.

5. Conclusions

In this study, various sintered AWGC samples were successfully prepared from the spray polysized raw powder. The morphologies and specific surface areas were examined by SEM and BET revealing porous structure. With the increasing sintering temperature, crystal growth decreases the porosities of AWGC samples for the lower value of the specific surface area, and the lower specific surface area results in high cell viability. Furthermore, all AWGC samples show good bioactivities from our XRD and SEM observations. In summary, the AWGC samples are considered promising bioceramic materials for orthopedic purposes.

Author Contributions: Conceptualization, S.-J.S.; methodology, A.B.W.; validation, S.-J.S., W.-L.Y., and H.S.N.; formal analysis, A.B.W. and H.S.N.; investigation, A.B.W.; data curation, A.B.W.; writing—original draft preparation, S.-J.S., A.B.W. and H.S.N.; writing—review and editing, S.-J.S. and H.S.N.; supervision, S.-J.S.; project administration, S.-J.S.; funding acquisition, W.-L.Y. All authors have read and agreed to the published version of the manuscript.

Data Availability Statement: The data that support the findings of this study are available from the corresponding author upon reasonable request.

Conflicts of Interest: The authors declare no conflict of interest.

References

1. Oonishi, H.; Hench, L.; Wilson, J.; Sugihara, F.; Tsuji, E.; Kushitani, S.; Iwaki, H. Comparative bone growth behavior in granules of bioceramic materials of various sizes. *J. Biomed. Mater. Res. B Appl. Biomater.* **1999**, *44*, 31–43. [CrossRef]
2. Saadaldin, S.A.; Rizkalla, A.S. Synthesis and characterization of wollastonite glass—Ceramics for dental implant applications. *Dent. Mater.* **2014**, *30*, 364–371. [CrossRef] [PubMed]
3. Kokubo, T.; Shigematsu, M.; Nagashima, Y.; Tashiro, M.; Nakamura, T.; Yamamuro, T.; Higashi, S. Apatite-and wollastonite-containg glass-ceramics for prosthetic application. *Bull. Inst. Chem. Res. Kyoto Univ.* **1982**, *60*, 260–268.
4. Yamamuro, T. Clinical Application of Glass Ceramics. In *Biomechanics and Biomaterials in Orthopedics*; Poitout, D.G., Ed.; Springer: Berlin/Heidelberg, Germany, 2016; pp. 153–157.
5. Kokubo, T. Bioactive glass ceramics: Properties and applications. *Biomaterials* **1991**, *12*, 155–163. [CrossRef]
6. Ito, M.; Abumi, K.; Moridaira, H.; Shono, Y.; Kotani, Y.; Minami, A.; Kaneda, K. Iliac crest reconstruction with a bioactive ceramic spacer. *Eur. Spine J. Eur.* **2005**, *14*, 99–102. [CrossRef] [PubMed]
7. Diba, M.; Goudouri, O.-M.; Tapia, F.; Boccaccini, A.R. Magnesium-containing bioactive polycrystalline silicate-based ceramics and glass-ceramics for biomedical applications. *Curr. Opin. Solid State Mater. Sci.* **2014**, *18*, 147–167.
8. Hossain, S.S.; Yadav, S.; Majumdar, S.; Krishnamurthy, S.; Pyare, R.; Roy, P. A comparative study of physico-mechanical, bioactivity and hemolysis properties of pseudo-wollastonite and wollastonite glass-ceramic synthesized from solid wastes. *Ceram. Int.* **2020**, *46*, 833–843. [CrossRef]
9. Radev, L.; Hristov, V.; Michailova, I.; Samuneva, B. Sol-gel bioactive glass-ceramics Part I: Calcium phosphate silicate/wollastonite glass-ceramics. *Open Chem.* **2009**, *7*, 317–321. [CrossRef]
10. Xue, M.; Ou, J.; Zhou, D.L.; Feng, D.; Yang, W.Z.; Li, G.; Liu, D.P.; Wang, Y.S. Preparation and properties of porous apatite-wollastonite bioactive glass-ceramic. *Key Eng. Mater.* **2007**, 169–172. [CrossRef]
11. Kokubo, T.; Ito, S.; Shigematsu, M.; Sakka, S.; Yamamuro, T. Mechanical properties of a new type of apatite-containing glass-ceramic for prosthetic application. *J. Mater. Sci.* **1985**, *20*, 2001–2004. [CrossRef]
12. Li, R.; Clark, A.; Hench, L. An investigation of bioactive glass powders by sol-gel processing. *J. Appl. Biomater.* **1991**, *2*, 231–239. [CrossRef]
13. Roman, J.; Padilla, S.; Vallet-Regi, M. Sol−gel glasses as precursors of bioactive glass ceramics. *Chem. Mater.* **2003**, *15*, 798–806. [CrossRef]
14. Padilla, S.; Roman, J.; Carenas, A.; Vallet-Regi, M. The influence of the phosphorus content on the bioactivity of sol–gel glass ceramics. *Biomaterials* **2005**, *26*, 475–483. [CrossRef]
15. Shih, C.; Chen, H.; Huang, L.; Lu, P.; Chang, H.; Chang, I. Synthesis and in vitro bioactivity of mesoporous bioactive glass scaffolds. *Mater. Sci. Eng. C* **2010**, *30*, 657–663. [CrossRef]

16. Shih, S.-J.; Chang, L.-Y.S.; Chen, C.-Y.; Borisenko, K.B.; Cockayne, D.J. Nanoscale yttrium distribution in yttrium-doped ceria powder. *J. Nanopart. Res.* **2009**, *11*, 2145–2152. [CrossRef]

17. Hench, L.L. Bioceramics: From concept to clinic. *J. Am. Ceram. Soc.* **1991**, *74*, 1487–1510.

18. Wallin, R.F. *A Practical Guide to ISO 10993-12: Sample Preparation and Reference Materials*; MDDI: Los Angeles, CA, USA, 1998.

19. Kitsugi, T.; Yamamuro, T.; Nakamura, T.; Kokubo, T. Bone bonding behavior of MgO-CaO-SiO$_2$-P$_2$O$_5$-CaF$_2$ glass (mother glass of AW-glass-ceramics). *J. Biomed. Mater. Res.* **1989**, *23*, 631–648. [CrossRef] [PubMed]

20. Shih, S.-J.; Chou, Y.-J.; Chien, I.-C. One-step synthesis of bioactive glass by spray pyrolysis. *J. Nanopart. Res.* **2012**, *14*, 1–8. [CrossRef]

21. Shih, S.-J.; Tzeng, W.-L.; Chou, Y.-J.; Chen, C.-Y.; Chen, Y.-J. The influence of phase separation on bioactivity of spray pyrolyzed bioactive glass. *J. Nanosci. Nanotechnol.* **2015**, *15*, 4688–4696. [CrossRef]

22. Kokubo, T.; Ito, S.; Sakka, S.; Yamamuro, T. Formation of a high-strength bioactive glass-ceramic in the system MgO-CaO-SiO$_2$-P$_2$O$_5$. *J. Mater. Sci.* **1986**, *21*, 536–540. [CrossRef]

23. Lagier, R.; Baud, C.-A. Magnesium whitlockite, a calcium phosphate crystal of special interest in pathology. *Pathol. Res. Pract.* **2003**, *199*, 329–335. [CrossRef] [PubMed]

24. German, R.M. *Sintering Theory and Practice*; Wiley: New York, NY, USA, 1996.

25. Hossain, A.A.; Mahmud, S.; Seki, M.; Kawai, T.; Tabata, H. Structural, electrical transport, and magnetic properties of Ni$_{1-x}$Zn$_x$Fe$_2$O$_4$. *J. Magn. Magn. Mater.* **2007**, *312*, 210–219. [CrossRef]

26. Addison, W.N.; Azari, F.; Sørensen, E.S.; Kaartinen, M.T.; McKee, M.D. Pyrophosphate inhibits mineralization of osteoblast cultures by binding to mineral, up-regulating osteopontin, and inhibiting alkaline phosphatase activity. *J. Biol. Chem.* **2007**, *282*, 15872–15883. [CrossRef] [PubMed]

27. Pioletti, D.P.; Takei, H.; Lin, T.; Van Landuyt, P.; Ma, Q.J.; Kwon, S.Y.; Sung, K.-L.P. The effects of calcium phosphate cement particles on osteoblast functions. *Biomaterials* **2000**, *21*, 1103–1114. [CrossRef]

28. Ningsih, H.S.; Tannesia, L.; Chen, H.-H.; Shih, S.-J. Fabrication, characterization and in vitro cytotoxicity of mesoporous β-tricalcium phosphate using the spray drying method. *Crystals* **2021**, *11*, 252. [CrossRef]